PHYSICAL REVIEW B **90**, 184427 (2014)

Spin Hall torque magnetometry of Dzyaloshinskii domain walls

Satoru Emori,[1] Eduardo Martinez,[2] Kyung-Jin Lee,[3,4] Hyun-Woo Lee,[5] Uwe Bauer,[1] Sung-Min Ahn,[1] Parnika Agrawal,[1] David C. Bono,[1] and Geoffrey S. D. Beach[1,*]

[1]*Department of Materials Science and Engineering, Massachusetts Institute of Technology, Cambridge, Massachusetts 02139, USA*
[2]*Departmento Física Aplicada, Universidad de Salamanca, Plaza de los Caidos s/n E-38008, Salamanca, Spain*
[3]*Department of Materials Science and Engineering, Korea University, Seoul 136-701, Korea*
[4]*KU-KIST Graduate School of Converging Science and Technology, Korea University, Seoul 136-713, Korea*
[5]*PCTP and Department of Physics, Pohang University of Science and Technology, Kyungbuk 790-784, Korea*

(Received 4 August 2013; revised manuscript received 1 November 2014; published 25 November 2014)

Current-induced domain wall motion in the presence of the Dzyaloshinskii-Moriya interaction (DMI) is experimentally and theoretically investigated in heavy-metal/ferromagnet bilayers. The angular dependence of the current-induced torque and the magnetization structure of Dzyaloshinskii domain walls are described and quantified simultaneously in the presence of in-plane fields. We show that the DMI strength depends strongly on the heavy metal, varying by a factor of 20 between Ta and Pa, and that strong DMI leads to wall distortions not seen in conventional materials. These findings provide essential insights for understanding and exploiting chiral magnetism for emerging spintronics applications.

DOI: 10.1103/PhysRevB.90.184427 PACS number(s): 75.60.Ch, 75.78.Fg, 75.70.Kw, 75.70.Cn

I. INTRODUCTION

Spin-orbit-driven phenomena at heavy-metal/ferromagnet (HM/FM) interfaces have become the focus of intense research efforts. The influence of spin-orbit coupling (SOC) on spin transport and magnetization textures leads to new fundamental behaviors that can be exploited in high-performance, low-power spintronic devices [1–23]. In HM/FM bilayers, Rashba [3,5,6] and spin Hall effects [7–9,14–16] can generate current-induced spin-orbit torques (SOTs) [24] potentially much stronger than conventional spin-transfer torques (STTs) [25]. In these same materials, SOC and broken inversion symmetry [15,16,26–30] can stabilize chiral spin textures such as spin spirals [26], skyrmions [27,30], and homochiral DWs [15,16,28,29] through the Dzyaloshinskii-Moriya interaction (DMI) [29–32]. The influence of SOTs on chiral spin textures has only begun to be explored, but recent work suggests spin torque from the spin Hall effect (SHE) can drive DMI-stabilized homochiral Néel DWs with very high efficiency [15,16]. The behavior of these Dzyaloshinskii DWs [31] is however not yet well understood, due in part to the difficulty of disentangling spin torques and spin textures in these materials.

Here we exploit the angular dependence of the SHE torque to quantify its role in DW dynamics while simultaneously probing the structure and energetics of Dzyaloshinskii DWs. We find that the DMI in HM/CoFe bilayers depends strongly on the HM, but its dependence is distinct from that of the SHE. The DMI exchange constant differs by a factor of ~20 between Ta and Pt, but has the same sign, whereas the SHE for these HMs is of similar magnitude but opposite sign. These results show that while the SHE and DMI both derive from spin-orbit coupling, they arise from distinct mechanisms in these materials and can be independently engineered. Moreover, we uncover a qualitatively new behavior exhibited by DWs in the presence of strong DMI, wherein torque applied to a DW rotates not just the DW moment, but tilts the entire DW line profile. We describe this unconventional behavior through analytical and micromagnetic modeling that accurately describes our experiments and permits quantitative extraction of the DMI strength in such materials. These results provide fundamental insight into interface-driven chiral magnetism and guidance for designing SOC-enabled spintronic devices.

II. EXPERIMENTS

We studied perpendicularly magnetized Pt/CoFe/MgO and Ta/CoFe/MgO nanostrips that served as conduits for DWs. Ta(3 nm)/Pt(3 nm)/CoFe(0.6 nm)/MgO(1.8/nm)/Ta(2 nm) and Ta(5 nm)/CoFe(0.6 nm)/MgO(1.8 nm)/Ta(2 nm) films were sputter-deposited onto Si/SiO_2 substrates at room temperature, as described in Ref. [15]. Vibrating sample magnetometry on continuous films revealed full out-of-plane remanent magnetization and in-plane (hard-axis) saturation fields $H_\perp \approx 3$ kOe for Ta/CoFe/MgO and $H_\perp \approx 5$ kOe for Pt/CoFe/MgO. The saturation magnetization M_s was $\approx$700 emu/cm^3 for both films.

The films were patterned using electron beam lithography and lift-off to produce nanostrips with Ta/Cu electrodes [Fig. 1(a)] in two separate lithographic steps. Using this device structure, DWs were nucleated by the Oersted field from a 30-ns long 50 mA current pulse injected through the nucleation line [connected to PG1 in Fig. 1(a)], and driven along the nanostrip by a combination of out-of-plane field H_z and electron current density [33] j_e [output by PG2 in Fig. 1(a)]. H_z was generated by an air-coil, whereas in-plane bias fields were generated by an iron-core electromagnet [34]. Magnetization reversal was detected locally with the polar magneto-optical Kerr effect (MOKE) using a ~3 μm laser spot. Most measured strips were 500 nm wide; some measurements were conducted on 1200-nm wide strips with identical results (see Appendix A).

Figure 1(b) shows magnetization switching probed near the center of a nanostrip as H_z was swept at 17 Hz in a triangular waveform. These measurements were obtained through signal averaging of 100 reversal cycles. The dotted curve corresponds

*gbeach@mit.edu

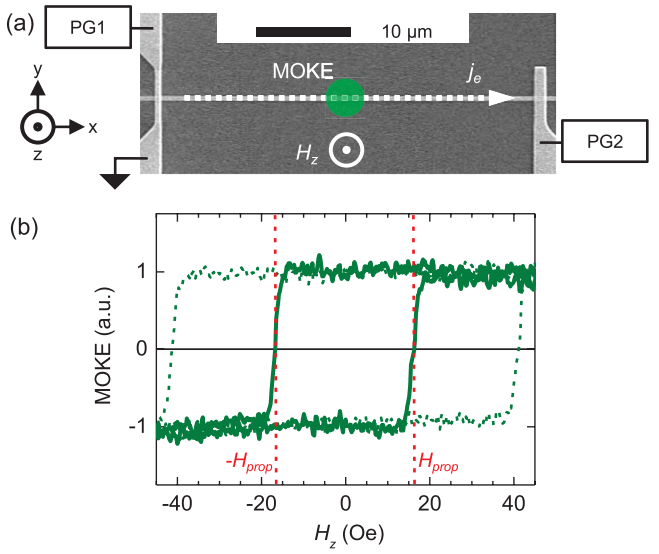

FIG. 1. (Color online) (a) Illustration of experimental setup superposed on a micrograph of a nanostrip device. Pulse generator 1 (PG1) outputs the DW nucleation pulse and PG 2 outputs j_e along the nanostrip. (b) Polar MOKE hysteresis loops obtained with DWs initialized by the nucleation pulse (solid curve) and without nucleation pulses (dotted curve). $H_{\rm prop}$ is indicated by red dotted lines.

to a simple hysteresis loop in the absence of nucleation pulses, such that the switching field corresponds to the threshold for random nucleation. The solid line in Fig. 1(b) shows a similar measurement obtained when short nucleation pulses were applied at the zero crossings of the swept field H_z. In this case, the switching field decreased significantly, and corresponds to the propagation field $H_{\rm prop}$ required to drive the nucleated DW through the defect potential landscape to the probe laser spot.

Figure 2 shows that $H_{\rm prop}$ varies linearly with j_e, indicating current acts as an easy-axis effective field $\vec{H}_{\rm eff} = \chi\, j_e \hat{z}$ that can assist or hinder DW propagation. Both nonadiabatic STT [2,35,36] and spin torque from the SHE [19–21,37] generate effective fields of this form, but differ in the dependence of χ on the DW configuration. For one-dimensional (1D) DWs with the usual Walker profile [31], $\chi_{\rm SHE} = \frac{\pi}{2}\chi^0_{\rm SHE}\cos(\Phi)$ for SHE torque, where Φ is the angle between the DW moment and the x axis. Here $\chi^0_{\rm SHE} = \hbar\theta_{\rm SH}/2\mu_0\,|e|\,M_s t$, where $\theta_{\rm SH}$, e, M_s, and t are the spin Hall angle, electron charge, saturation magnetization, and ferromagnet thickness, respectively. By contrast, nonadiabatic STT [25] is independent of Φ, with $\chi_{\rm STT} = \pm\hbar\beta P/2\mu_0\,|e|\,\Delta M_s$, where Δ is the DW width, β is the nonadiabicity parameter, and positive (negative) corresponds to up-down (down-up) DWs such that current drives them in the same direction.

The relative contributions of STT and SHE torque to χ can be determined by applying in-plane fields, which by themselves do not move DWs but can reorient Φ. Figure 2 shows $H_{\rm prop}$ versus j_e for Ta/CoFe/MgO without and with bias fields along $\hat{x}$ and $\hat{y}$. With no in-plane field [Fig. 2(d)], j_e assists DW motion along the electron flow direction, identically for up-down and down-up DWs. Under large $H_x < 0$ [Fig. 2(e)], χ changes sign for down-up DWs, while for up-down DWs χ is unchanged. For large $H_x > 0$, the opposite behavior is observed, while for both DW types, χ tends to zero under large $|H_y|$ [Fig. 2(f)].

The sign reversal of χ under H_x, and its vanishing under H_y, show that the symmetry of $\vec{H}_{\rm eff}$ is consistent with the Slonczewski-like damping-like torque from the SHE. Under large $|H_y|$ Bloch DWs [$\cos(\Phi) = 0$] are preferred [Fig. 2(c)], and the contribution to χ from the SHE should vanish [Fig. 2(f)]. In this case only $\chi_{\rm STT}$ remains, which according to Fig. 2(f) is negligibly small. Under large H_x Néel DWs [$\cos(\Phi) = \pm 1$] are stabilized with opposite chirality for up-down and down-up transitions [Fig. 2(b)]. In this case $\vec{H}_{\rm eff}$ from the SHE should drive these DWs in opposite directions, as observed experimentally in Fig. 2(e). Therefore, since at $H_x = H_y = 0$ the SHE torque drives up-down and down-up DWs identically in the same direction [Fig. 2(d)], they must be spontaneously Néel with oppositely oriented internal moments arranged in a left-handed chiral texture [Fig. 2(a)], consistent with an internal chiral effective field arising from the DMI [15,28].

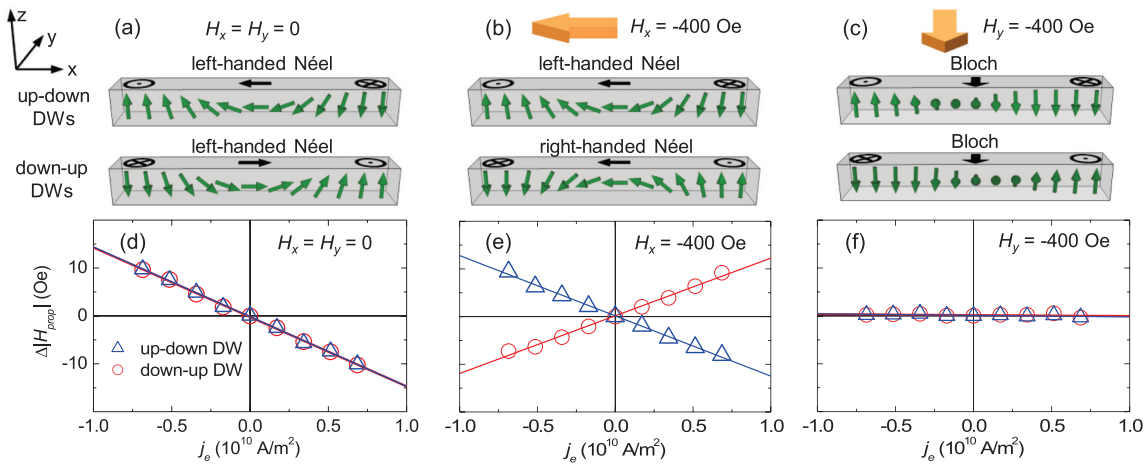

FIG. 2. (Color online) (a)–(c) Illustrations of DWs under (a) zero in-plane field, (b) longitudinal field H_x, and (c) transverse field H_y. (d)–(f) Change in $H_{\rm prop}$ versus j_e in Ta/CoFe/MgO corresponding to (a)–(c).

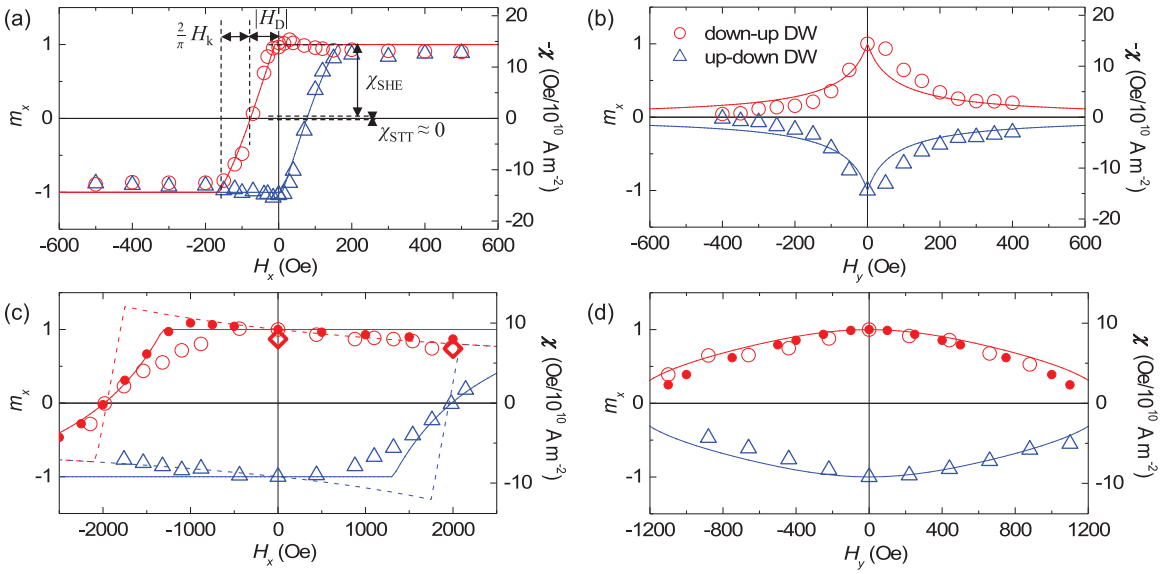

FIG. 3. (Color online) Measured χ (open symbols), analytically computed longitudinal component m_x of DW moment (solid curves) and micromagnetically computed χ (solid circles). (a) and (b) Ta/CoFe/MgO under (a) H_x and (b) H_y; $-\chi$ plotted to account for negative spin Hall angle. (c) and (d) Pt/CoFe/MgO under (c) H_x and (d) H_y. Dotted curves in (c) show analytical correction to χ due to domain canting for H_x parallel to H_D. Open diamonds in (c) denote χ obtained from micromagnetic simulations of field and current-driven DW propagation with edge roughness; uncertainty is of the order of the symbol size.

III. RESULTS

A. Weak DMI case—Ta/CoFe/MgO

Figures 3(a) and 3(b) show the full field dependence of χ in Ta/CoFe/MgO. These data were fitted to the form $\chi_{SHE} = \frac{\pi}{2}\chi^0_{SHE}\cos(\Phi)$, where the dependence of the angle Φ between the DW moment and the x axis was computed as a function of H_x and H_y using a 1D DW model with DMI. In this model [31] the DW surface energy density σ in the presence of in-plane fields can be written

$$\frac{\sigma}{2\Delta\mu_0 M_s} = \frac{1}{2}H_k\cos^2(\Phi) - \frac{\pi}{2}H_D\cos(\Phi) - \frac{\pi}{2}H_x\cos(\Phi) - \frac{\pi}{2}H_y\sin(\Phi) + H_\perp, \quad (1)$$

where H_k, H_D, and $H_\perp$ are the DW shape anisotropy field, the DMI effective field, and the perpendicular anisotropy field, respectively. The shape anisotropy term accounts for the DW demagnetizing energy, and has an easy axis along $\hat{y}$ that prefers Bloch DWs [38]. The DMI effective field takes the form $H_D = \pm D/\mu_0 M_s\Delta$ directed normal to the DW, where D is the effective DMI constant and $+$ $(-)$ corresponds to up-down (down-up) DWs. This term prefers homochiral Néel DWs.

By minimizing σ with respect to Φ, one obtains analytical expressions for the dependence of $\cos(\Phi)$, and hence χ_{SHE}, on H_x, H_y. Since $\cos(\Phi)$ is simply the x component m_x of the normalized DW internal moment, the SHE can thus be used to probe the DW configuration under in-plane applied fields. In the case of H_x we find

$$\cos(\Phi) = m_x = \begin{cases} +1 & (H_D + H_x) > \frac{2}{\pi}H_k \\ \pi(H_D + H_x)/2H_k & -\frac{2}{\pi}H_k < (H_D + H_x) < \frac{2}{\pi}H_k \\ -1 & (H_D + H_x) < -\frac{2}{\pi}H_k \end{cases}. \quad (2)$$

The dependence of $\cos(\Phi) = m_x$ on H_y can likewise be found through the relation

$$-H_k m_x\sqrt{1-m_x^2} + \frac{\pi}{2}H_D\sqrt{1-m_x^2} - \frac{\pi}{2}H_y m_x = 0. \quad (3)$$

The solid lines in Figs. 3(a) and 3(b) show fits of the data to $\chi_{SHE} = \frac{\pi}{2}\chi^0_{SHE}\cos(\Phi)$, with $\cos(\Phi)$ determined through Eqs. (2) and (3). This simple model accounts quantitatively for the experimental results, yielding best-fit parameters $H_k = 110$ Oe, $|H_D| = 80$ Oe, and $\frac{\pi}{2}\chi^0_{SHE} = 15\,\mathrm{Oe}/10^{10}\mathrm{A/m^2}$, and a chirality corresponding to left-handed Néel DWs.

A remarkable aspect about Fig. 3(a) is that the spin torques and DW energy terms can be directly and independently read from the figure even without recourse to fitting. The curve for each DW is analogous to a biased hard-axis hysteresis loop, where the horizontal breadth of the transition gives the DW shape anisotropy field H_k, and the zero-crossing field gives H_D [see labels in Fig. 3(a)]. Likewise, the spin torques can be read directly from the vertical axis. The amplitude of the measured χ versus H_x curve is proportional to θ_{SH}, and the vertical offset is proportional to βP. The symmetry of the SHE effective field can thus be used to probe the orientation of the DW moment

$\hat{m}$ under H_x or H_y, from which the angular-dependent DW energy terms can be extracted in analogy with conventional magnetometry.

The measured $\chi^0_{\rm SHE}$ corresponds to an effective spin Hall angle $\theta_{\rm SH} \approx -0.11$, in agreement with Ref. [8]. Any contribution to χ by $\chi_{\rm STT}$ would give rise to a field-independent vertical offset in Fig. 3(a). We find no such offset within the experimental uncertainty, which implies an upper limit $\beta P = 0.02 \pm 0.02$. This is in contrast to $\beta P > 1$ inferred in similar materials where variations under in-plane fields were not considered [2,35,36]. These results disentangle SHE and STT in such materials, and show that here nonadiabatic STT plays a negligible role.

In addition to the effective fields H_k, H_D, the data in Figs. 3(a) and 3(b) can be combined with conventional magnetometry to yield both the DMI constant D and the ferromagnetic exchange constant A. The shape anisotropy field for Néel DWs [39] is $H_k \approx M_s t \ln(2)/\pi\Delta$. Here $\Delta = \sqrt{A/K_{u,\rm eff}}$ is the DW width, and $K_{u,\rm eff}$ is the effective perpendicular anisotropy energy density. Using M_s and $K_{u,\rm eff}$ determined by vibrating sample magnetometry, we find $\Delta \approx 10.6$ nm, which yields $A \approx 1.0 \times 10^{-11}$ J/m and $D \approx -0.053\,{\rm mJ/m^2}$, where the sign indicates left-handedness. These simple measurements hence provide quantitative insight into every relevant micromagnetic parameter simultaneously, which has never before been achieved.

B. Strong DMI case—Pt/CoFe/MgO

Figures 3(c) and 3(d) show χ versus in-plane fields for Pt/CoFe/MgO, extracted from the slope of $H_{\rm prop}$ versus j_e as was done for Ta/CoFe/MgO. The behavior is qualitatively similar to that in Ta/CoFe/MgO, with χ changing sign under large H_x, and decreasing smoothly with increasing $|H_y|$. However, much larger fields $|H_x| \approx 2000$ Oe are required to reverse χ [Fig. 3(c)], and under H_y the decline in χ is quite gradual [Fig. 3(d)], suggesting that here the DMI is much stronger. As described below, in the case of strong DMI, the usual rigid 1D DW model cannot adequately describe the response of DWs to torques. First, experimentally probing strong Dzyaloshinskii DWs requires application of large in-plane fields, which not only rotate the DW moment but also cant the magnetization in the domains. Second, since strong DMI pins the DW moment to the DW normal, a torque on the DW moment tends to rotate the DW normal in the film plane, causing the DW to tilt with respect to the nanostrip axis. Below we first treat these effects separately using an analytical treatment that provides physical insight, and then use a general micromagnetic approach that accounts for both effects numerically in order to quantitatively fit the data in Figs. 3(c) and 3(d) and accurately extract the DMI strength.

C. Domain canting and Thiele effective forces

When H_x, H_y are comparable to the perpendicular anisotropy field $H_\perp \approx 5000$ Oe, the domains cant significantly from $\pm\hat{z}$ and are no longer collinear. Since the magnetization rotation across the DW is then different from 180°, the Walker ansatz no longer applies, and the 1D equations of motion in Ref. [31] must be amended.

The domain wall (DW) profile in the presence of an in-plane field was derived in Refs. [40–43], from which we obtain the Thiele equations (see Appendix B) that describe the DW dynamics in terms of position q and wall angle Φ. The Thiele force equation under longitudinal field H_x is given by

$$\frac{\alpha}{\Delta}\left(1 - \frac{2h\xi}{\sqrt{1-h^2}}\right)\dot{q} \mp \sqrt{1-h^2}\dot{\Phi} = \mp\gamma\sqrt{1-h^2}H_z \mp 2\gamma\xi H_{\rm SHE}\cos\Phi, \quad (4)$$

and the Thiele torque equation is given by

$$\mp\frac{\sqrt{1-h^2}}{\Delta}\dot{q} - \alpha\sqrt{1-h^2}(\sqrt{1-h^2}+2h\xi)\dot{\Phi} = 2\gamma\sqrt{1-h^2}\xi H_x\sin\Phi \mp \gamma\frac{2D}{\Delta\mu_0 M_S}\xi\sin\Phi - \sqrt{1-h^2}\gamma\frac{K_s}{\mu_0 M_S}(\sqrt{1-h^2}+2h\xi)\sin 2\Phi. \quad (5)$$

Here the upper (lower) sign corresponds to the up-down (down-up) DWs, $H_{\rm SHE} = \frac{\pi}{2}\chi^0_{\rm SHE} j_e$ and $\xi = \tan^{-1}[(1-h)/\sqrt{1-h^2}]$, with $h \equiv H_x/H_\perp$.

In the case of a transverse field H_y, we define $h \equiv H_y/H_\perp$ and find that the Thiele force equation is unchanged from (4), while the torque equation becomes

$$\mp\frac{\sqrt{1-h^2}}{\Delta}\dot{q} - \alpha\sqrt{1-h^2}(\sqrt{1-h^2}+2h\xi)\dot{\Phi} = -2\gamma\sqrt{1-h^2}\xi H_y\cos\Phi \mp \gamma\frac{2D}{\Delta\mu_0 M_S}\xi\sin\Phi - \sqrt{1-h^2}\gamma\frac{K_s}{\mu_0 M_S}(\sqrt{1-h^2}+2h\xi)\sin 2\Phi. \quad (6)$$

By setting $h = 0$ in Eqs. (5) and (6), one recovers the conventional Thiele equations without domain canting given in Ref. [31].

One sees from Eq. (4) that the spin Hall effective field is equivalent to an easy-axis applied field given by

$$H_z^{\rm eff} = \frac{2\xi}{\sqrt{1-h^2}}H_{\rm SHE}\cos\Phi \quad (7)$$

so that

$$\chi_{\rm SHE} = \frac{2\xi}{\sqrt{1-h^2}}\chi^0_{\rm SHE}\cos\Phi. \quad (8)$$

With no in-plane field, Eq. (8) reduces to $\chi_{\rm SHE} = \frac{\pi}{2}\chi^0_{\rm SHE}\cos(\Phi)$ as above, but domain canting due to applied in-plane fields modifies current-induced effective field from the SHE.

The dotted curves in Fig. 3(c) show $\chi_{\rm SHE}$ versus H_x computed in this model, where the dependence of $\cos(\Phi)$ on H_x can be expressed analytically (see Appendix B). We used the measured $H_\perp$ and set $H_k = 150$ Oe based on Taresenko's expression [39], leaving H_D as the only free parameter. Taking $|H_D| = 1800$ Oe for left-handed DWs, this model reproduces the zero-crossing field of χ versus H_x. Interestingly, domain canting leads to the counterintuitive result that in the field range where the DW remains Néel, χ is diminished when H_x is parallel to the DW moment, and is enhanced when H_x opposes the internal DW moment. Hence, one should expect

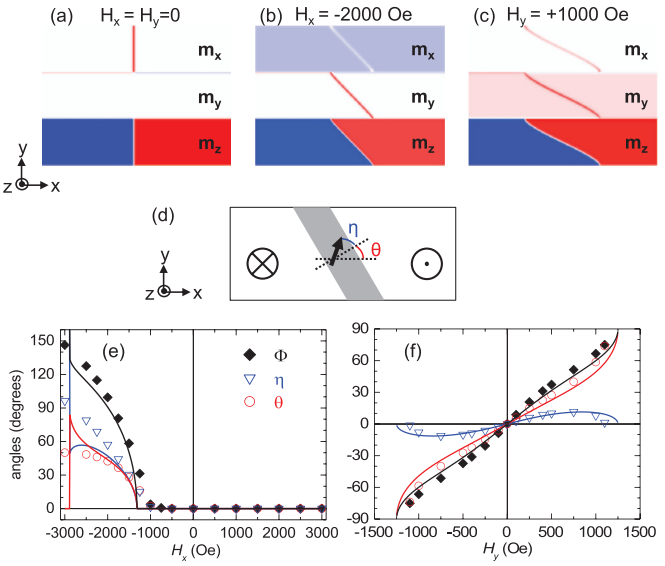

FIG. 4. (Color online) (a)–(c) Micromagnetic snapshots of down-up DWs under (a) zero in-plane field, (b) H_x against the DMI, and (c) H_y. The three Cartesian components of $\boldsymbol{m}$ are shown, with red $= +1$, white $= 0$, and blue $= -1$. (d) Definitions of angles η and θ. (e) and (f) DW rotation parametrized by $\Phi = \eta + \theta$ under (e) H_x and (f) H_y for micromagnetic (symbols) and analytical (lines) calculations.

a quasilinear variation of χ about $H_x = 0$, the slope of which yields the DW chirality.

While this model explains the observed reduction of χ when H_x is parallel to H_D, it predicts a relatively abrupt reversal of DW chirality when $H_x \approx -H_D$, whereas experimentally, χ changes sign much more gradually. This behavior arises from a tilting of the DW line profile in the plane due to strong DMI, which we treat in the following section.

D. Domain wall tilting under strong DMI

The micromagnetic simulations in Fig. 4 reveal the source of the discrepancy between the data in Figs. 3(c) and 3(d) and the rigid 1D model. These simulations were performed using custom code [44] modified to include the DMI (Appendix B) with $D = -1.2\,\mathrm{mJ/m^2}$, as determined in the next section. The computed sample was 500 nm wide and 0.6 nm thick, and its length was 2048 nm with appropriate boundary conditions imposed to simulate an infinitely long strip. The material parameters used were: exchange constant $A = 10^{-11}\,\mathrm{J/m}$; saturation magnetization $M_s = 7 \times 10^5\,\mathrm{A/m}$; and perpendicular magnetocrystalline anisotropy constant $K_u = 4.8 \times 10^5\,\mathrm{J/m^3}$. These parameters corresponded to experimentally determined values for Pt/CoFe/MgO, except for A, which was determined experimentally for Ta/CoFe/MgO in Sec. III A and is assumed to be the same for Pt/CoFe/MgO. This value of A gives a DW width $\Delta = \sqrt{A/K_{u,\mathrm{eff}}} = 7.6$ nm, where $K_{u,\mathrm{eff}} = K_u - \frac{1}{2}\mu_0 M_s^2$.

At $H_x = H_y = 0$, the DW spans the nanostrip orthogonally to minimize elastic line energy [Fig. 4(a)], but under in-plane applied fields that tend to rotate the DW moment, the DW line tilts dramatically in the $x - y$ plane [Figs. 4(b) and 4(c)]. This remarkable behavior can be understood from simple energy minimization under strong DMI. The Zeeman energy tends to align the DW moment $\hat{m}$ with the applied field, while the DMI prefers $\hat{m}$ to remain normal to the DW. If the DW line were fixed rigidly in position, then $\hat{m}$ would rotate progressively towards the applied field at the expense of the DMI energy. However, if the DW line itself rotates in the $x - y$ plane, $\hat{m}$ can follow the applied field while dragging with it the DW normal, thereby reducing the DMI energy penalty. Despite the energy cost of increasing the DW length, DW tilting should lower the net energy if the DMI is sufficiently strong.

Indeed, unexplained tilting of current-driven DWs was recently observed [11] in Pt/Co/Ni/Co/TaN. This behavior is fully consistent with strong DMI, which should lead to DW tilting whenever a torque tends to rotate the DW moment in the plane. Under the large currents ($\sim 10^{12}\,\mathrm{A/m^2}$) used in Ref. [11], the SHE effective field exerts a torque on the DW moment about the z axis which, due to strong DMI at the Pt/Co interface [16] should cause dynamical tilting of the DW normal, consistent with Ref. [11]. In the present case, we apply much smaller currents ($\sim 10^{10}\,\mathrm{A/m^2}$) and examine quasistatic DW motion (thermally activated propagation through fine-scale disorder), so that the propagating DW configuration under H_x, H_y is determined by total energy minimization.

We modeled DW tilting analytically by parametrizing the DW by two angles [Fig. 4(d)]: η, the angle between $\hat{m}$ and the DW normal, and θ, the tilting of the DW normal away from the x axis. We assume the DW remains straight, so $\hat{m}$ is everywhere inclined by $\Phi = \eta + \theta$ from the x axis, and domain canting is neglected for simplicity. The DW energy E under H_x and H_y is then modified from the form in Eq. (1) as

$$E \propto \frac{1}{\cos\theta}\left[\frac{1}{2}H_k\cos^2(\eta) - \frac{\pi}{2}H_D\cos(\eta) - \frac{\pi}{2}H_x\cos(\eta+\theta) - \frac{\pi}{2}H_y\sin(\eta+\theta) + H_\perp\right], \quad (9)$$

which yields the quasistatic DW configuration through minimization with respect to η and θ. The out-of-plane anisotropy field is given by $H_\perp = 2K_{u,\mathrm{eff}}/\mu_0 M_s$ and accounts for the DW internal energy. In the case of strong DMI, H_k can be neglected when $H_k \ll |H_D|$.

Minimizing Eq. (9) with respect to θ and η yields the equilibrium DW configuration under H_x and H_y. In the case of H_x, one finds

$$\sin\theta = \frac{\frac{\pi}{2}H_x\sin\eta}{-\frac{1}{2}H_k\cos^2\eta + \frac{\pi}{2}H_D\cos\eta - H_\perp} \quad (10)$$

and

$$\sin\eta = \frac{\frac{\pi}{2}H_x\sin(\eta+\theta)}{H_k\cos\eta - \frac{\pi}{2}H_D}. \quad (11)$$

For H_x far from $H_x = -H_D$, the physical solutions are $\eta = 0$, π, and $\theta = 0$. This corresponds to the DW moment orienting along the x axis ($m_x = \pm 1$) with no tilting of the DW normal.

Under transverse field H_y, minimizing Eq. (9) with respect to η and θ yields

$$\sin\theta = \frac{\frac{\pi}{2}H_y\cos\eta}{\frac{1}{2}H_k\cos^2\eta - \frac{\pi}{2}H_D\cos\eta + H_\perp} \quad (12)$$

and

$$\sin\eta = \frac{\frac{\pi}{2}H_y\cos(\eta+\theta)}{H_k\cos\eta - \frac{\pi}{2}H_D}. \quad (13)$$

The solid curves in Figs. 3(c) and 3(d) show $m_x = \cos(\Phi)$ versus H_x and H_y, which reproduces the gradual reversal (reduction) of χ under H_x (H_y) observed experimentally. The parameters used here are $|H_D| = 2800$ Oe, with left-handed chirality, and $H_\perp = 6300$ Oe, close to the measured value. The tilt angles versus H_x, H_y agree qualitatively with the full micromagnetic results, as seen in Figs. 4(e) and 4(f). We note that the longitudinal field required to null χ significantly underestimates H_D when DMI is strong, since DW tilting allows Φ to rotate more readily than if the DW normal remained fixed.

E. Full micromagnetic treatment of Thiele effective forces

To treat domain canting and DW tilting simultaneously, we performed full 2D micromagnetic simulations (see Appendixes C and D) of the equilibrium DW structure versus H_x and H_y (Fig. 4), and computed $\chi_{\rm SHE}$ numerically from the Thiele expressions [45]

$$\begin{aligned}\vec{H}^{\rm DW}_{\rm SHE} &= \frac{H_{\rm SHE}}{2}\frac{1}{w}\int_{-\infty}^{\infty}\int_0^w\left[(\hat{\rm m}\times\hat{\rm y})\frac{\partial\hat{\rm m}}{\partial x}\right]dydx\hat{z}\\ &\equiv H_{\rm SHE}I_{\rm SHE}\hat{z},\\ \vec{H}^{\rm DW}_{z} &= \frac{H_z}{2}\frac{1}{w}\int_{-\infty}^{\infty}\int_0^w\left[\hat{z}\frac{\partial\hat{\rm m}}{\partial x}\right]dydx\hat{z} \equiv H_zI_z\hat{z} \quad (14)\end{aligned}$$

for the effective fields from the SHE and H_z, respectively. Under the usual 1D Walker ansatz for the DW structure, Eqs. (14) reduce to $H^{\rm DW}_{\rm SHE} = \frac{\pi}{2}H_{\rm SHE}\cos\Phi$ and $H^{\rm DW}_z = H_z$ so that $\chi_{\rm SHE} = \frac{\pi}{2}\chi^0_{\rm SHE}\cos(\Phi)$ as expected. In the case of a general DW profile, the SHE acts like an easy-axis applied field $(I_{\rm SHE}/I_z)\,H_{\rm SHE}$, so that $\chi_{\rm SHE} = (I_{\rm SHE}/I_z)\,\chi^0_{\rm SHE}$.

We used Eqs. (14) to fit the in-plane field-dependence of χ in Figs. 3(c) and 3(d), by micromagnetically computing the DW structure as a function of H_x and H_y and numerically computing $\chi_{\rm SHE} = (I_{\rm SHE}/I_z)\,\chi^0_{\rm SHE}$ using Eqs. (14). This fit used only two free parameters: the effective spin Hall angle $\theta_{\rm SH}$, which determines the vertical scale factor, and the DMI exchange constant D.

We first determined $\theta_{\rm SH} \approx +0.07$ from the value of χ measured at $H_x = H_y = 0$ in Figs. 3(c) and 3(d), which agrees well with $\theta_{\rm SH}$ for Pt in Ref. [7]. We then varied the single parameter D to best match the field dependence of the normalized quantity $\chi/\chi(H_x = H_y = 0)$, while holding all other micromagnetic parameters fixed at their measured values. This one-parameter fit reproduces the experimental data remarkably well with the best-fit value $D = -1.2\,{\rm mJ/m^2}$ [solid circles in Figs. 3(c) and 3(d)].

There remains some discrepancy between data and fit when H_x opposes H_D, which we attribute to local dispersion of D due to interface disorder. The micromagnetic simulations in Fig. 4(e) predict a sudden onset of DW tilting at a critical H_x, where χ begins to drop [Fig. 3(c)]. Local dispersion in D would tend to broaden this transition by allowing the DW moment to rotate at lower H_x in some regions due to locally smaller D. Refining the model to include dispersion is however beyond the present scope.

IV. DISCUSSION

The results in Fig. 3 show that DW motion in Pt/CoFe/MgO and Ta/CoFe/MgO can be accounted for quantitatively by the SHE and DMI, and that the variation of the current-induced effective field with in-plane applied fields provides a means to conveniently extract these parameters. In the case of weak DMI, a simple 1D model suffices for analyzing the experimental data, but in the case of strong DMI, where large in-plane fields are required to probe the stiffness of the homochiral Néel DWs, a numerical approach is required. Nonetheless, as shown above, Eqs. (14) provide a general framework to numerically fit the data in terms of just two free parameters $\theta_{\rm SH}$ and D that are essentially uncorrelated.

We note that the calculations of χ used to fit the data in the analyses above are based on the equilibrium DW structure, whereas experiments are performed under conditions of thermally activated DW propagation near the depinning threshold. Therefore, it could be expected that pinning could distort the DW and lead to deviations from the models used for fitting the data. However, the experimental analysis is based on measuring the average propagation field measured over many repeated propagation cycles across a relatively long propagation distance, thus probing the full ensemble of disorder and thermally activated fluctuations. Deviations from the nominal DW line profile due to random distortions during propagation should hence average towards zero in the experimental determination of χ. Indeed, we verified through finite-temperature micromagnetic simulations of DW propagation under realistic conditions of disorder [46] that the tilting predicted in Fig. 4 under static equilibrium is preserved on average during thermally activated propagation in the presence of edge roughness, whereas in the absence of strong DMI no net tilting is observed.

The presence of a single strong pinning site at an edge could lead to preferential tilting of the DW in one direction that would be repetitive from cycle to cycle, systematically influencing the current-induced effective field. However, if the measured propagation field were due to a single dominant defect, the current-induced depinning efficiency would necessarily vary randomly and significantly from device to device, and from position to position along a given device, depending on the location and strength of this dominant, random pinning site. In Appendix A we show measurements of $H_{\rm prop}$ versus j_e, for several nominally identical structures, for a range of structures with different widths, and measurements using different field-sweep frequencies (and hence propagation time scales). In all of these measurements the extracted χ is identical within experimental uncertainty, indicating that this parameter is a robust measure of the current-induced effective field.

Finally, we determined $H_{\rm prop}$ and $j_{\rm prop}$ through dynamical micromagnetic simulations of DW propagation with edge roughness, shown in detail in Appendix D, to verify that our quasistatic analysis of χ reproduces the full micromagnetics treatment. In these simulations, we used micromagnetic parameters for Pt/CoFe/MgO extracted from the analysis presented above, and included a random edge roughness with

a characteristic grain size of $D_g = 4$ nm. The propagation thresholds for field-driven and current-driven motion were determined separately, and their ratio used to determine χ. With an effective spin Hall angle $\theta_{SH} = +0.07$ used in the simulations, the ratio H_{prop}/j_{prop} [open diamonds in Fig. 3(c)] matches well with the experimentally measured χ and with χ calculated from the static micromagnetic DW structure via Eqs. (14) [solid points in Figs. 3(c) and 3(d)]. These results further validate our approach to fitting the data numerically using the micromagnetically computed equilibrium DW structure via Eqs. (14).

V. CONCLUSIONS

The DMI constant D takes the same sign for Pt/CoFe/MgO and Ta/CoFe/MgO but differs in magnitude by a factor of 20, while the spin Hall angle θ_{SH} alternates in sign from Pt to Ta but the magnitudes are within a factor of 2. This suggests that the DMI and Slonczewski-like SOT, though related through SOC, derive from different microscopic mechanisms in these materials and can hence be independently tuned. In the case of strong DMI, the frequently used 1D model fails qualitatively to describe DW motion in the presence of large in-plane fields or strong torques on the DW moment. Both domain canting and DW tilting must be treated in full in order to quantitatively extract the DMI strength from experiments.

The DMI in Pt/CoFe/MgO is remarkably strong, comparable to that in ultrathin epitaxial layers grown on single crystal substrates [26–28]. This suggests the feasibility of realizing more complex spin textures [26,27,30,32] such as spin spirals and skyrmions in robust thin-film heterostructures. These should emerge for $|H_D|/H_\perp > 2/\pi$ [31] not far from $|H_D|/H_\perp \approx 0.45$ measured here for Pt/CoFe/MgO. The possibility to engineer spin torques and spin textures, using materials amenable to practical device integration, presents new opportunities for high-performance spintronics applications.

ACKNOWLEDGMENTS

This work was supported in part by the National Science Foundation under NSF-ECCS-1128439. Devices were fabricated using instruments in the MIT Nanostructures Laboratory, the Scanning Electron-Beam Lithography facility at the Research Laboratory of Electronics, and the Center for Materials Science and Engineering at MIT. S.E. acknowledges financial support by the NSF Graduate Research Fellowship Program. The work by E.M. was supported by projects MAT2011-28532-C03-01 from the Spanish government, SA163A12 from Junta de Castilla y Leon, and WALL FP7-PEOPLE-2013-ITN (608031) from the European Commission. The work by K.J.L. was supported by the NRF (No. 2013R1A2A2A01013188), and the work by H.W.L. by the NRF (No. 2011-0030046).

APPENDIX A: DOMAIN WALL PROPAGATION FIELD GOVERNED BY FINE-SCALE DEFECTS

Time-of-flight domain wall (DW) velocity measurements (Fig. 5 and Refs. [15,47]) indicate a uniform average DW velocity along the strip under a constant driving current. For example, even at a low current density $j_e \sim 10^{10}$A/m^2, DWs moved uniformly on average at ~0.01 m/s [Figs. 5(b) and 5(d)]. Plots of the logarithm of the DW velocity against $j_e^{-1/4}$

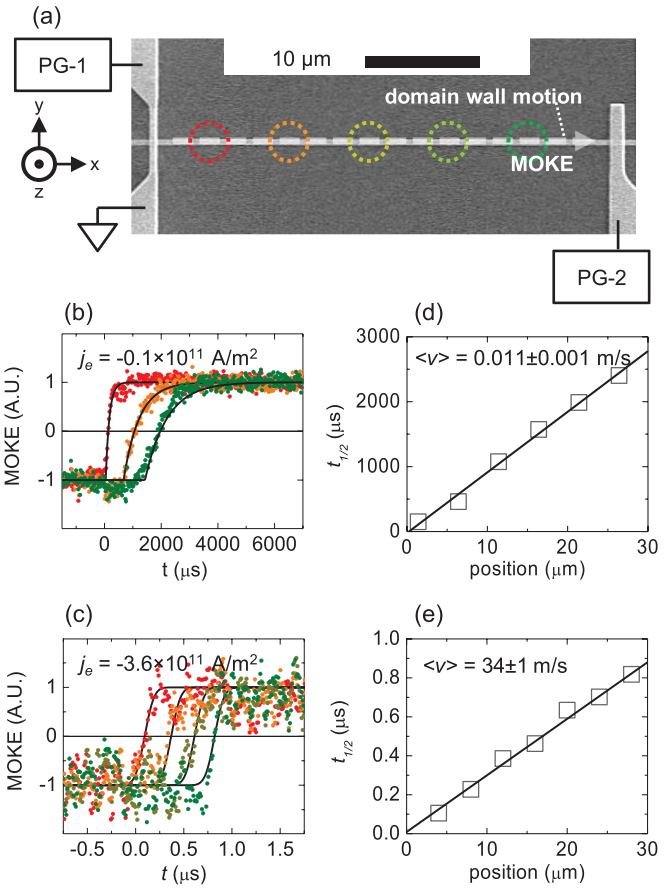

FIG. 5. (Color online) (a) Schematic of the time-of-flight DW motion measurement. The MOKE laser spot is placed at several positions along the nanostrip. At each position, an averaged MOKE transient (magnetization switching due to DW switching as a function of time) is measured. (b) and (c) Normalized MOKE transients at different positions in a Pt/CoFe/MgO strip at (b) a small driving current and (c) large driving current. (d) and (e) DW arrival time $t_{1/2}$ (time at which the zero crossing of the normalized MOKE transient occurs) at a small driving current corresponding to (b) and large driving current corresponding to (c), plotted against measured position.

and $H_z^{-1/4}$ (Fig. 6) yield linear relationships, suggesting DW motion is well described by two-dimensional creep scaling [48,49]. Therefore, for the results shown in this study, H_{prop} is governed by DW pinning from nanoscale inhomogeneity (e.g., film roughness, grain boundaries, etc.) distributed throughout each nanostrip, rather than from a single dominant defect in a nanostrip. This latter case would lead to discontinuities in the position versus time measurements, which is not observed. The typical H_{prop} in the absence of j_e and in-plane bias fields was ~20 Oe in Ta/CoFe/MgO and Pt/CoFe/MgO nanostrips.

Because H_{prop} is a measure of thermally activated DW motion, the baseline H_{prop} at $j_e = 0$ may vary from sample to sample [Figs. 7(a), 7(b), and 8(a)] or with the sweep rate of the driving field H_z [Fig. 8(b)]. H_{prop} is modified by a constant current $j_e \neq 0$ injected during the H_z sweep. The change in H_{prop} scales linearly with the value of j_e, as shown in Figs. 7 and 8, indicating that j_e is equivalent to a dc offset in H_z that drives DWs. The slope $\chi = \Delta H_{prop}/\Delta j_e$ is essentially the

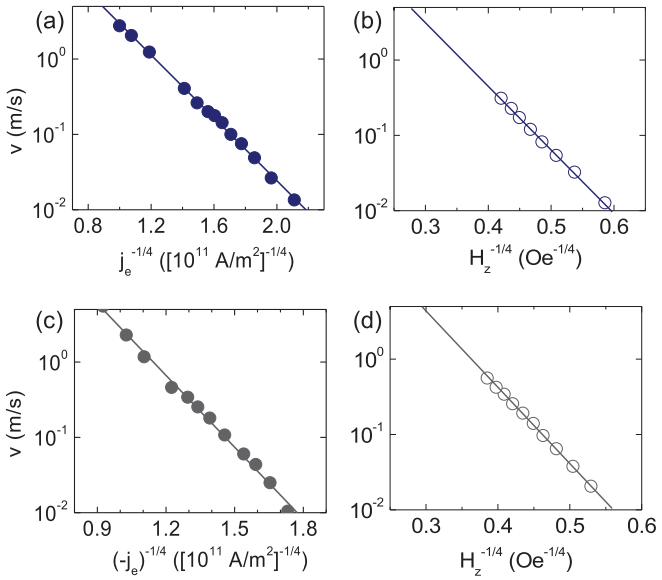

FIG. 6. (Color online) DW velocity plotted against $j_e^{-1/4}$ and $H_z^{-1/4}$ for (a) and (b) Ta/CoFe/MgO and (c) and (d) Pt/CoFe/MgO. The lower maximum measured velocity driven by H_z (b) and (d) is due to random domain nucleation.

same (varying at most by ∼10%) for different samples and sweep rates (Figs. 7 and 8). Thus, χ is a robust measure of the current-induced effective field, from which we can quantify the spin Hall effect and the x component of the DW magnetic moment m_x.

In-plane fields (H_x and H_y) cant the domain magnetization away from the out-of-plane easy axis. With increasing H_x or H_y, the nucleation field $H_{\rm nuc}$ decreases, thereby making it more difficult to isolate DW propagation from random nucleation of reverse domains (i.e., $H_{\rm nuc}$ approaches $H_{\rm prop}$). This was especially problematic in measurements of Pt/CoFe/MgO, for which large in-plane fields were required to produce a considerable change in χ (or m_x). The results shown in Figs. 3(c) and 3(d) were obtained from 1200-nm wide Pt/CoFe/MgO strips, which typically had larger $H_{\rm nuc}$ than 500-nm wide strips. $H_{\rm nuc}$ also remained greater than the $H_{\rm prop}$ over a greater range of in-plane fields by conducting these measurements with a faster field sweep rate ≈500 Oe/ms (compared to ≈10 Oe/ms used for Ta/CoFe/MgO) and the MOKE laser placed ≈5 μm away from the nucleation line

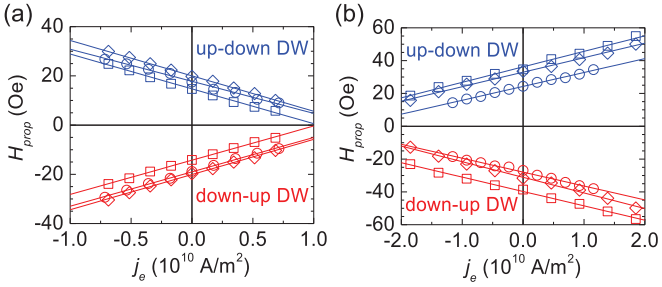

FIG. 7. (Color online) Change in the DW propagation field $H_{\rm prop}$ with respect to electron current density j_e in nominally identical samples of (a) Ta/CoFe/MgO and (b) Pt/CoFe/MgO.

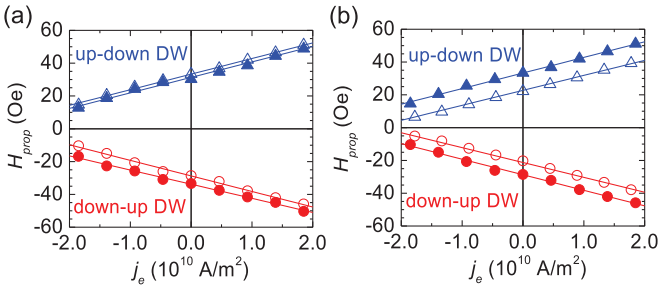

FIG. 8. (Color online) Change in the DW propagation field $H_{\rm prop}$ with respect to electron current density j_e in Pt/CoFe/MgO nanostrips (a) with different widths (empty symbol: 500 nm; filled symbol: 1200 nm), and (b) under different field sweep rates and MOKE laser positions (empty symbol: ≈10 Oe/ms, ≈20 μm away from the nucleation line; filled symbol: ≈500 Oe/ms, ≈5 μm away from the nucleation line).

(compared to ≈20 μm for Ta/CoFe/MgO). The difference in the sample width or the measurement parameters did not affect the slope χ, as shown in Fig. 8.

APPENDIX B: DOMAIN WALL PROFILE UNDER LARGE IN-PLANE FIELDS

The DW profile in the presence of the in-plane longitudinal field was derived in Refs. [40–43] as

$$\theta(x,t) = \sin^{-1}\left(h + \frac{1-h^2}{\cosh\{[x-q(t)]/\Delta\}+h}\right),$$
$$\Phi(x,t) = \Phi(t) \quad \text{for} \quad x > q(t),$$
$$\theta(x,t) = \pi - \sin^{-1}\left(h + \frac{1-h^2}{\cosh\{[x-q(t)]/\Delta\}+h}\right),$$
$$\Phi(x,t) = \Phi(t) \quad \text{for} \quad x \leqslant q(t), \tag{B1}$$

where θ is the polar angle, Φ is the azimuthal angle, q is the DW center position, $h \equiv H_x/H_\perp$ is the normalized external longitudinal field, and $H_\perp$ is the effective perpendicular anisotropy field. Here Δ is the DW width, defined as

$$\Delta = \frac{\sqrt{A/K_{u,\rm eff}}}{\sqrt{[1+(K_s/K_{u,\rm eff})\cos^2\Phi](1-h^2)}} \tag{B2}$$

where A is the exchange stiffness constant, $K_{u,\rm eff} = \frac{1}{2}\mu_0 M_s H_\perp$ is the effective perpendicular anisotropy energy density, and $K_s = \frac{1}{2}\mu_0 M_s H_k$ is the DW (magnetostatic) shape anisotropy energy density. Equation (B2) shows that the DW width depends on the in-plane field as well as the DW angle Φ. Here we neglect its dependence on Φ for simplicity (by assuming that $K_s/K_{u,\rm eff}$ is small), and apply the rigid DW approximation for a given h in order to derive the Thiele equations below. Within the rigid DW limit, we note that Eqs. (B1) and (B2) describe the DW profile regardless of the direction of in-plane field, so that these expressions are likewise applicable for transverse applied field by redefining $h \equiv H_y/H_\perp$. We obtain Thiele's equations from Eqs. (B1) and (B2), as given by Eqs. (4)–(6).

Since the experiments are performed under quasistatic conditions of DW depinning and creep, we obtain Φ from the steady state solution ($\dot{q} = \dot{\Phi} = 0$) for the torque equation

[Eqs. (5) or (6)]. In the case of H_x, the torque equation, Eq. (5), may be solved analytically, yielding

$$\cos\Phi = -\xi\frac{\pm D - \sqrt{1-h^2}\mu_0 H_x M_S \Delta}{K_s \Delta\sqrt{1-h^2}(\sqrt{1-h^2}+2h\xi)}. \tag{B3}$$

Here + (−) corresponds to up-down (down-up) DWs. Equation (B3) can be rewritten in terms of effective fields as

$$\cos\Phi = -\xi\frac{\pm H_D - \sqrt{1-h^2}H_x}{\frac{1}{2}H_k\sqrt{1-h^2}(\sqrt{1-h^2}+2h\xi)}. \tag{B4}$$

Where the sign of H_D alternates between up-down and down-up DWs. These expressions, restricted to the range $-1 \leqslant \cos\Phi \leqslant 1$, were used to generate the dotted curve in Fig. 3(c).

We note that strictly speaking Eq. (B1) is analytically integrable to obtain the Thiele equations only in the case $|\cos\Phi| = 1$ corresponding to Néel DWs. Therefore, Eqs. (B3) and (B4) are not analytically exact solutions to the model. Nonetheless, these equations provide the range of h over which the ansatz of a Néel DW holds, such that whenever $|\cos\Phi| > 1$ in these expressions, one fixes $\cos\Phi = \pm 1$ as appropriate and the derived Thiele equations are self-consistent with the assumed DW profile. The width of the transition regions depicted by the dotted curves in Fig. 3(c) is therefore accurate within this model, but the exact form of the transition will deviate from that predicted by Eqs. (B3) and (B4) and plotted in Fig. 3(c). Importantly, the predicted variation of χ with h in the field ranges where the DW is fully Néel is analytically well motivated.

APPENDIX C: DETAILS OF MICROMAGNETICS IMPLEMENTATION

Energy and effective field—The equilibrium states were computed by integrating the total energy density ε over the sample $E = \int_V \varepsilon dV$. Apart from the standard exchange $\varepsilon_{\text{exch}}$, perpendicular magnetocrystalline anisotropy $\varepsilon_{\text{ani},u}$ (uniaxial with easy axis along the z direction), magnetostatic ε_{dmg}, and external field ε_{ext} contributions, it also accounts for the DMI ε_{DMI}. In the continuous approach for thin films (with dimensions L_x, w, t along the Cartesian axes, and with $t \ll w, L_x$), the variations of the magnetization along the z axis can be neglected, and the total energy density can be expressed as [31,50]

$$\begin{aligned}\varepsilon &= \varepsilon_{\text{exch}} + \varepsilon_{\text{ani},u} + \varepsilon_{dmg} + \varepsilon_{\text{ext}} + \varepsilon_{\text{DMI}} \\ &= A\left[\left(\frac{\partial\vec{m}}{\partial x}\right)^2 + \left(\frac{\partial\vec{m}}{\partial y}\right)^2\right] + K_u[1-(\vec{m}\cdot\vec{u}_k)^2] \\ &\quad - \frac{1}{2}\mu_0 M_s \vec{H}_{dmg}\cdot\vec{m} - \mu_0 M_s \vec{H}_{\text{ext}}\cdot\vec{m} \\ &\quad + D\left[\left(m_z\frac{\partial m_x}{\partial x} - m_x\frac{\partial m_z}{\partial x}\right) + \left(m_z\frac{\partial m_y}{\partial y} - m_y\frac{\partial m_z}{\partial y}\right)\right],\end{aligned} \tag{C1}$$

where (m_x, m_y, m_z) are the local Cartesian components of the magnetization vector $\vec{m}(\vec{r}) = \vec{M}(\vec{r})/M_s$ normalized to the saturation magnetization M_s, A is the exchange constant, K_u is the perpendicular magnetocrystalline anisotropy constant, and D is the DMI parameter. $\vec{H}_{dmg}(\vec{r})$ is the magnetostatic field computed from the magnetization distribution through the magnetostatics equations, and $\vec{H}_{\text{ext}} = (H_x, H_y, 0)$ is the externally applied in-plane magnetic field.

Similar to conventional micromagnetic formalism [51], the static equilibrium state can be obtained from the calculus of variations ($\delta E = 0$) and expressed as a zero-torque condition in terms of a local effective field $\vec{H}_{\text{eff}}(\vec{r})$, as

$$\vec{m}(\vec{r}) \times \vec{H}_{\text{eff}}(\vec{r}) = 0 \tag{C2}$$

for each point $\vec{r}$ of the sample, where the local effective field $\vec{H}_{\text{eff}}(\vec{r})$ is

$$\begin{aligned}\vec{H}_{\text{eff}}(\vec{r}) &= -\frac{1}{\mu_0 M_s}\frac{\delta\varepsilon}{\delta\vec{m}} \\ &= \frac{2A}{\mu_0 M_s}\nabla^2\vec{m} + \frac{2K_u}{\mu_0 M_S} m_z \vec{u}_z + \vec{H}_{dmg} + \vec{H}_{\text{ext}} \\ &\quad + \frac{2D}{\mu_0 M_S}\left[\frac{\partial m_z}{\partial x}\vec{u}_x + \frac{\partial m_z}{\partial y}\vec{u}_y - \left(\frac{\partial m_x}{\partial x} + \frac{\partial m_y}{\partial y}\right)\vec{u}_z\right].\end{aligned} \tag{C3}$$

The magnetostatic field $\vec{H}_{dmg}(\vec{r})$ is evaluated by means of the fast Fourier transform (FFT) and the zero padding technique using Newell's expressions for the magnetostatics [52]. See Ref. [44] for further details.

Boundary conditions—In the absence of DMI, the exchange interaction imposes boundary conditions at the surfaces of the sample [53] such that the magnetization vector does not change along the surface normal $\vec{n}$, that is

$$\frac{\partial\vec{m}}{\partial n} = 0, \tag{C4}$$

where $\partial/\partial n$ indicates the derivative in the outside direction normal to the surface of the sample. However, in the presence of the DMI, this boundary condition has to be replaced by

$$\frac{d\vec{m}}{dn} = \frac{D}{2A}\vec{m}\times(\vec{n}\times\vec{u}_z). \tag{C5}$$

Solver—The sample was discretized using a 2D mesh with a lateral cell size of 4 nm. For each applied in-plane field, Eq. (C2) together with Eqs. (C3) and (C5) were iteratively solved by means of a conjugate gradient solver [54]. The equilibrium state is assumed to be achieved when this condition is reached with a maximum error of $|\vec{m}(\vec{r}) \times \vec{H}_{\text{eff}}(\vec{r})| < 10^{-5}$ for all computational cells.

Simulation of domain wall displacement—Domain wall motion assisted by a spatially uniform current density along the x axis $\vec{j}_a = j_a\vec{u}_x$, is studied by solving the augmented Landau-Lifshitz-Gilbert equation [23,31]

$$\begin{aligned}\frac{d\vec{m}}{dt} &= -\gamma_0\vec{m}\times\vec{H}_{\text{eff}} + \alpha\vec{m}\times\frac{d\vec{m}}{dt} \\ &\quad + \gamma_0\frac{\hbar\theta_{\text{SH}} j_a}{2e\mu_0 M_s L_z}\vec{m}\times(\vec{m}\times\vec{u}_y),\end{aligned} \tag{C6}$$

where γ_0 is the gyromagnetic ratio, $\hbar$ is the reduced Planck constant, e is the electric charge, and μ_0 is the permeability of free space. The first term on the right-hand side of Eq. (C6)

describes the local magnetization precession around the local effective field $\vec{H}_{\text{eff}}$, which includes exchange, magnetostatic, uniaxial perpendicular magnetocrystalline anisotropy, external field $\vec{H}_{\text{ext}} = (H_x, H_y, H_z)$, and DMI contributions as described above. The second term accounts for the dissipation with the dimensionless Gilbert damping parameter set to $\alpha = 0.3$. The last term on the right-hand side of Eq. (C6) is the Slonczewski-like torque due to the SHE with $\theta_{\text{SH}} = +0.07$. The sample was discretized using a 2D mesh with a lateral cell size of 4 nm, and Eq. (C6) was numerically solved by means of a fourth Runge-Kutta algorithm with a time step of 65 fs.

APPENDIX D: MICROMAGNETIC SIMULATION OF DW PROPAGATION FIELD AND PROPAGATION CURRENT

Micromagnetic simulations were performed to evaluate the propagation field H_{prop} and the propagation current j_{prop}, and from them the field-to-current correspondence (efficiency) χ in the presence of in-plane longitudinal field parallel to the equilibrium DMI-stabilized internal DW moment. The disorder to impede DW motion was incorporated with an edge roughness with a typical grain size of $D_g = 4$ nm on both sides of the strip (see Ref. [55] for further details). Such random disorder is qualitatively consistent with nanoscale defects distributed throughout experimentally measured strips (as described in Appendix A). The dimensions of the computed sample are length $L_x = 2800$ nm, width $w = 160$ nm, and thickness $t = 0.6$ nm. We used micromagnetic parameters corresponding to the Pt/CoFe/MgO sample: $M_s = 7 \times 10^5$ A/m, $K_u = 4.8 \times 10^5$ J/m^3, $A = 10^{-11}$ J/m, $\alpha = 0.3$, and $\theta_{\text{SH}} \approx +0.07$. The smaller strip width was chosen to save computational time

The "propagation values" H_{prop} and j_{prop} are defined as the minimum field (along z axis) and the minimum current density (along the x axis) required to promote sustained DW motion along a distance of 1.2 μm. Below these threshold values, the DW displaces some distance from its initial position until reaching a final position where it remains pinned. The present study was performed for an up-down wall with left-handed chirality, so that the internal DW moment points along the negative x axis at rest. The aims of this study are to

(1) Verify that the efficiency χ determined from Thiele effective forces computed for the equilibrium micromagnetic DW configuration agrees with the value determined from micromagnetically simulated DW propagation (depinning) in the presence of disorder (which might distort the DWs and change the efficiency)

(2) Verify micromagnetically the decrease of the DW efficiency observed in the experimental measurements and predicted from Thiele force analysis of equilibrium DW structures, when an in-plane longitudinal field H_x is applied in the same direction as the equilibrium DW moment (preferred by DMI).

We considered purely field-driven motion and purely current-driven motion separately, and varied field (current) in steps of 0.5 Oe (0.05×10^{11}A/m^2) near the depinning threshold in order to determine H_{prop} and j_{prop}, respectively. Figure 9 shows representative DW position versus time curves that illustrate the behaviour just below and just above the (zero-temperature) depinning thresholds.

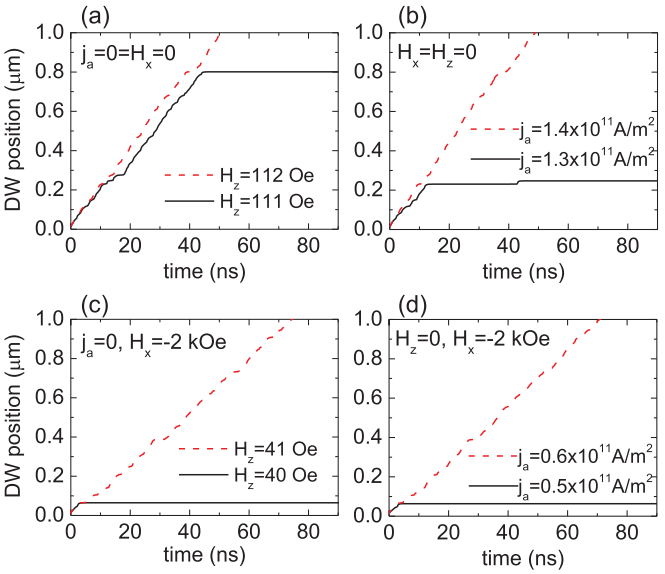

FIG. 9. (Color online) Micromagnetically computed DW displacement driven by H_z or j_a in a nanostrip with edge roughness under $H_x = 0$ and $H_x = -2000$ Oe oriented parallel to the DMI-stabilized DW moment.

The efficiency χ is defined in the same manner as in the experiments, that is the ratio of H_{prop} to j_{prop} which yields

$$\chi_{\mu M}(H_x = 0; D_g = 4\text{ nm}; T = 0) = \frac{H_{\text{prop}}(j_a = H_x = 0)}{j_{\text{prop}}(H_z = H_x = 0)} \approx \frac{112\text{ Oe}}{0.14 \times 10^{12}\text{ A/m}^2} = \frac{8.0\text{ Oe}}{10^{10}\text{ A/m}^2}$$

for $H_x = 0$, and

$$\chi_{\mu M}(H_x = -2000\text{ Oe}; D_g = 4\text{ nm}; T = 0) = \frac{H_{\text{prop}}(j_a = 0; H_x = -2000\text{ Oe})}{j_{\text{prop}}(H_z = 0; H_x = -2000\text{ Oe})} \approx \frac{41\text{ Oe}}{0.06 \times 10^{12}\text{ A/m}^2} = \frac{6.8\text{ Oe}}{10^{10}\text{ A/m}^2}$$

for $H_x = -2000$ Oe.

This value is around a 15% smaller than in the absence of in-plane field, and it is also in good agreement with experimental observations and with the micromagnetically computed efficiency based on numerical analysis of the equilibrium DW configurations. The absolute values of χ agree with the effective field expected from a spin Hall angle of $+0.07$ used in the simulations. These micromagnetic results are depicted by open diamonds in Fig. 3(c).

We note that in addition to the slight reduction of χ under H_x, explained above analytically due to the domain canting effect, there is a substantial reduction in the absolute pinning strength (i.e., both H_{prop} and j_{prop} are significantly reduced under large H_x, compared to the $H_x = 0$ case). This effect arises from the variation in the DW energy density under in-plane fields, which was computed analytically and applied to the case of DW creep in Ref. [56].

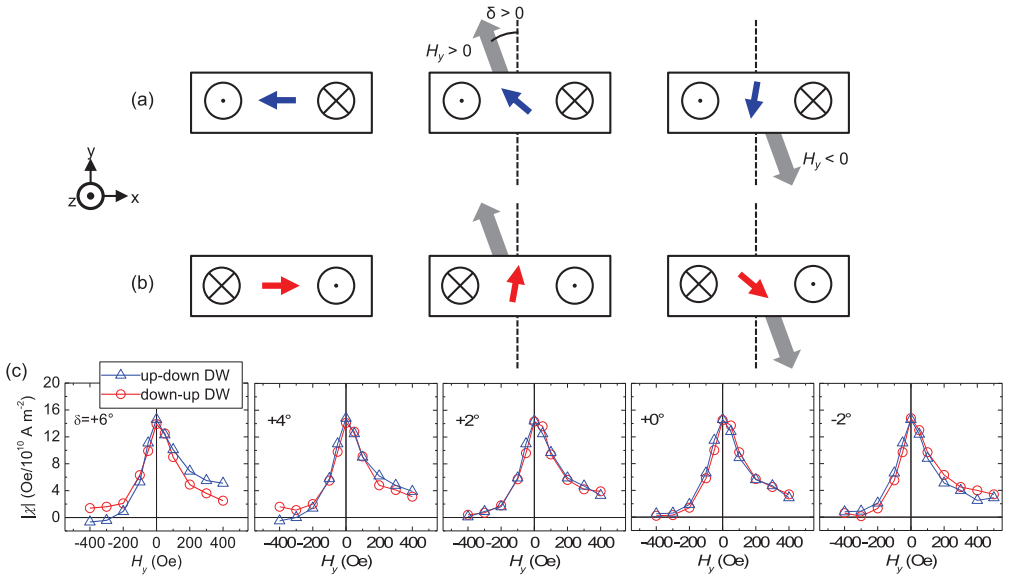

FIG. 10. (Color online) (a) and (b) Illustrations of the internal moment orientation for the (a) up-down DW and (b) down-up DW under transverse field H_y with a misalignment δ. (c) Efficiency χ versus H_y at different misalignments δ.

APPENDIX E: ASYMMETRY IN χ UNDER H_y IN Ta/CoFe/MgO

In Fig. 3 the current-induced effective z-axis field $H_z^{\text{eff}} = \chi j_e$ was extracted from the slope of the propagation field versus current (its sign determined by considering the direction that up-down or down-up DWs are driven by current). The data show χ is asymmetric with respect to H_y in Ta/CoFe/MgO [Fig. 3(b)]. For both up-down and down-up DWs, the decrease in χ is larger for $H_y < 0$.

We verified that this asymmetry does not arise from misalignment of H_y, by measuring χ (defined here as the slope of H_{prop} versus j_e) under various nominal field misalignments δ. As shown in Fig. 10(c), the intentional misalignment does not eliminate the asymmetry. However, χ changes differently for up-down and down-up DWs under field misalignment, e.g., for $H_y > 0$ and $\delta = 6^\circ$, it is clear that χ increases for up-down DWs, whereas it decreases for down-up DWs. For up-down DWs [Fig. 10(a)], the longitudinal $(-x)$ component of misaligned $H_y > 0$ aligns the internal moment closer to the DMI-stabilized $-x$ orientation, so that the efficiency to the spin Hall effect does not decrease as much. By contrast, for the down-up DW [Fig. 10(b)], the same misaligned $H_y > 0$ rotates the moment farther away

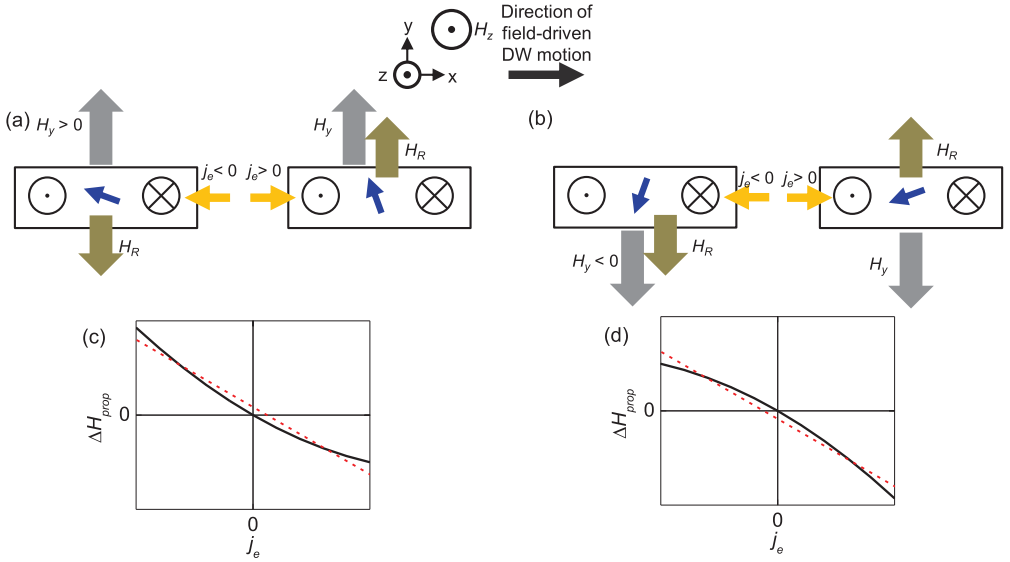

FIG. 11. (Color online) (a) and (b) Illustrations of the effect of the Rashba field H_R on the DW magnetization for (a) $H_y > 0$ and (b) $H_y < 0$. (c) and (d) Illustrations of the effect H_R would have on measurements of $\Delta H_{\text{prop}}/j_e$ (solid black curve) for (c) $H_y > 0$ and (d) $H_y < 0$. Note that even if a Rashba field were present, it would not account for the asymmetry in Fig. 10 since $H_y > 0$ and $H_y < 0$ would exhibit the same slope if a linear fit were used to fit in ΔH_{prop} against j_e (dotted red line). Note also that the curvature in these schematically represented data is not present in the actual experimental data, such as are shown in Figs. 2(d)–2(f).

from the DMI-stabilized $+x$ orientation, thereby reducing the spin Hall torque efficiency more than for the up-down DW.

The current-induced Oersted field or the transverse field from the Rashba effect may be expected to play a role in the asymmetry under H_y. In particular, previous studies have reported large apparent transverse-field-like torques in Ta/CoFe(B)/MgO [12,15,57], which could arise from the transverse Rashba field H_R. (By contrast, in Pt/CoFe/MgO, the Rashba-like field is negligibly small [15].) H_R scales linearly with electron current density j_e, and the direction of H_R reverses if j_e is reversed. Therefore, under a fixed H_y, the transverse H_R should enhance or hinder the rotation of the DW moment with H_y, depending on the direction of j_e [Figs. 11(a) and 11(b)]. This would lead to a nonlinear relation between ΔH_{prop} and j_e [Figs. 11(c) and 11(d)], in which the slope (efficiency χ) increases with larger $|j_e|$ when H_R and H_y are antiparallel, and decreases when H_R and H_y are parallel. Because $|j_e|$ was small at $\sim 10^{10}\text{A/m}^2$ in our measurements, this nonlinearity was negligible, and ΔH_{prop} versus j_e could be fit linearly. The linear slopes, and hence χ, would be the same for $H_y > 0$ and $H_y < 0$, as illustrated in a schematic representation of the effect H_R would have on ΔH_{prop} versus j_e shown in Figs. 11(c) and 11(d).

The current-induced field from the Rashba effect, or any other effective transverse field that scales linearly with j_e, cannot account for the asymmetry in the efficiency χ versus H_y, for the following reasons:

(1) The nonlinear relation between ΔH_{prop} and j_e, expected under a strong Rashba field, is not observed in the experimental data [Figs. 2(d)–2(f), 7, and 8].

(2) Even if this nonlinear relation (i.e., Rashba field) were present, χ would be identical for both polarities of H_y (Fig. 11).

In these experiments, an out-of-plane driving field H_z is applied, which acts to depin the DW and drive it along the nanostrip, with the SHE effective field either assisting or impeding the field-driven motion. Although the experiment is close to the quasistatic regime due to the low current densities and long time scales, the propagation field nonetheless exerts a torque on the DW moment as the DW moves. This torque is proportional to $\hat{m} \times H_z\hat{z}$. In the experiments, the sign of H_z is reversed to drive up-down and down-up DWs in the same direction along the nanostrip for detection by MOKE. Since $\hat{m}$ changes sign also for up-down and down-up DWs due to the chirality, the field torque tends to cant the DW moment in the same direction along the y axis for up-down and down-up DWs (Fig. 12). In the depinning field measurements, when H_y is aligned with the H_z-induced projection of $\hat{m}$ along y, the depinning efficiency is more easily reduced than when H_y is oriented in the opposite direction (see Figs. 11 and 12).

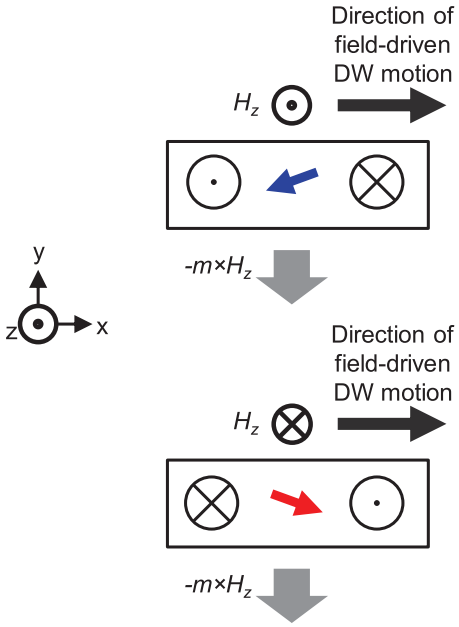

FIG. 12. (Color online) Slight rotation of the internal DW moment due to the H_z-induced torque. Both the up-down and down-up DWs move quasistatically in the $+x$ direction.

[1] T. A. Moore, I. M. Miron, G. Gaudin, G. Serret, S. Auffret, B. Rodmacq, A. Schuhl, S. Pizzini, J. Vogel, and M. Bonfim, Appl. Phys. Lett. **93**, 262504 (2008).

[2] I. M. Miron, P.-J. Zermatten, G. Gaudin, S. Auffret, B. Rodmacq, and A. Schuhl, Phys. Rev. Lett. **102**, 137202 (2009).

[3] I. M. Miron, G. Gaudin, S. Auffret, B. Rodmacq, A. Schuhl, S. Pizzini, J. Vogel, and P. Gambardella, Nat. Mater. **9**, 230 (2010).

[4] U. H. Pi, K. Won Kim, J. Y. Bae, S. C. Lee, Y. J. Cho, K. S. Kim, and S. Seo, Appl. Phys. Lett. **97**, 162507 (2010).

[5] I. M. Miron, T. Moore, H. Szambolics, L. D. Buda-Prejbeanu, S. Auffret, B. Rodmacq, S. Pizzini, J. Vogel, M. Bonfim, A. Schuhl, and G. Gaudin, Nat. Mater. **10**, 419 (2011).

[6] I. M. Miron, K. Garello, G. Gaudin, P.-J. Zermatten, M. V. Costache, S. Auffret, S. Bandiera, B. Rodmacq, A. Schuhl, and P. Gambardella, Nature (London) **476**, 189 (2011).

[7] L. Liu, O. J. Lee, T. J. Gudmundsen, D. C. Ralph, and R. A. Buhrman, Phys. Rev. Lett. **109**, 096602 (2012).

[8] L. Liu, C.-F. Pai, Y. Li, H. W. Tseng, D. C. Ralph, and R. A. Buhrman, Science **336**, 555 (2012).

[9] C.-F. Pai, L. Liu, Y. Li, H. W. Tseng, D. C. Ralph, and R. A. Buhrman, Appl. Phys. Lett. **101**, 122404 (2012).

[10] S. Emori, D. C. Bono, and G. S. D. Beach, Appl. Phys. Lett. **101**, 042405 (2012).

[11] K.-S. Ryu, L. Thomas, S.-H. Yang, and S. S. P. Parkin, Appl. Phys. Express **5**, 093006 (2012).

[12] J. Kim, J. Sinha, M. Hayashi, M. Yamanouchi, S. Fukami, T. Suzuki, S. Mitani, and H. Ohno, Nat. Mater. **12**, 240 (2013).

[13] X. Fan, J. Wu, Y. Chen, M. J. Jerry, H. Zhang, and J. Q. Xiao, Nat. Commun. **4**, 1799 (2013).

[14] P. P. J. Haazen, E. Murè, J. H. Franken, R. Lavrijsen, H. J. M. Swagten, and B. Koopmans, Nat. Mater. **12**, 299 (2013).

[15] S. Emori, U. Bauer, S.-M. Ahn, E. Martinez, and G. S. D. Beach, Nat. Mater. **12**, 611 (2013).

[16] K.-S. Ryu, L. Thomas, S.-H. Yang, and S. Parkin, Nat. Nanotechnol. **8**, 527 (2013).

[17] T. Koyama, H. Hata, K.-J. Kim, T. Moriyama, H. Tanigawa, T. Suzuki, Y. Nakatani, D. Chiba, and T. Ono, Appl. Phys. Express **6**, 033001 (2013).

[18] K. Garello, I. M. Miron, C. O. Avci, F. Freimuth, Y. Mokrousov, S. Blügel, S. Auffret, O. Boulle, G. Gaudin, and P. Gambardella, Nat. Nanotechnol. **8**, 587 (2013).

[19] X. Wang and A. Manchon, Phys. Rev. Lett. **108**, 117201 (2012).

[20] K.-W. Kim, S.-M. Seo, J. Ryu, K.-J. Lee, and H.-W. Lee, Phys. Rev. B **85**, 180404 (2012).

[21] P. M. Haney, H.-W. Lee, K.-J. Lee, A. Manchon, and M. D. Stiles, Phys. Rev. B **87**, 174411 (2013).

[22] E. Martinez, J. Appl. Phys. **111**, 033901 (2012).

[23] E. Martinez and G. Finocchio, IEEE Trans. Magn. **49**, 3105 (2013).

[24] A. Brataas, A. D. Kent, and H. Ohno, Nat. Mater. **11**, 372 (2012).

[25] A. Thiaville, Y. Nakatani, J. Miltat, and Y. Suzuki, Europhys. Lett. **69**, 990 (2005).

[26] M. Bode, M. Heide, K. von Bergmann, P. Ferriani, S. Heinze, G. Bihlmayer, A. Kubetzka, O. Pietzsch, S. Blügel, and R. Wiesendanger, Nature (London) **447**, 190 (2007).

[27] S. Heinze, K. von Bergmann, M. Menzel, J. Brede, A. Kubetzka, R. Wiesendanger, G. Bihlmayer, and S. Blügel, Nat. Phys. **7**, 713 (2011).

[28] M. Heide, G. Bihlmayer, and S. Blügel, Phys. Rev. B **78**, 140403 (2008).

[29] G. Chen, J. Zhu, A. Quesada, J. Li, A. T. N'Diaye, Y. Huo, T. P. Ma, Y. Chen, H. Y. Kwon, C. Won, Z. Q. Qiu, A. K. Schmid, and Y. Z. Wu, Phys. Rev. Lett. **110**, 177204 (2013).

[30] A. Fert, V. Cros, and J. Sampaio, Nat. Nanotechnol. **8**, 152 (2013).

[31] A. Thiaville, S. Rohart, É. Jué, V. Cros, and A. Fert, Europhys. Lett. **100**, 57002 (2012).

[32] O. A. Tretiakov and A. Abanov, Phys. Rev. Lett. **105**, 157201 (2010).

[33] Current densities were estimated by assuming current flow only through the CoFe layer and the adjacent heavy metal layer, so that the effective conductive thickness was 5.6 nm for Ta/CoFe/MgO and 3.6 nm for Pt/CoFe/MgO. We neglected current shunting in the bottom Ta seed layer in the Pt/CoFe/MgO, as sputtered Ta is at least 5 times more resistive than Pt.

[34] We estimate the misalignment of the in-plane field to be less than $\sim 2°$. The out-of-plane component of the field misalignment was calibrated through the offset in the DW propagation field in the nanostrip or the nucleation field of a nearby 20 μm square film.

[35] L. San Emeterio Alvarez, K.-Y. Wang, S. Lepadatu, S. Landi, S. J. Bending, and C. H. Marrows, Phys. Rev. Lett. **104**, 137205 (2010).

[36] J.-C. Lee, K.-J. Kim, J. Ryu, K.-W. Moon, S.-J. Yun, G.-H. Gim, K.-S. Lee, K.-H. Shin, H.-W. Lee, and S.-B. Choe, Phys. Rev. Lett. **107**, 067201 (2011).

[37] A. V. Khvalkovskiy, V. Cros, D. Apalkov, V. Nikitin, M. Krounbi, K. A. Zvezdin, A. Anane, J. Grollier, and A. Fert, Phys. Rev. B **87**, 020402 (2013).

[38] T. Koyama, D. Chiba, K. Ueda, K. Kondou, H. Tanigawa, S. Fukami, T. Suzuki, N. Ohshima, N. Ishiwata, Y. Nakatani, K. Kobayashi, and T. Ono, Nat. Mater. **10**, 194 (2011).

[39] S. V. Tarasenko, A. Stankiewicz, V. V. Tarasenko, and J. Ferré, J. Magn. Magn. Mater. **189**, 19 (1998).

[40] J. Kaczér and R. Gemperle, Czech. J. Phys. B **11**, 510 (1961).

[41] V. L. Sobolev, H. L. Huang, and S. C. Chen, J. Magn. Magn. Mater. **147**, 284 (1995).

[42] O. Boulle, L. D. Buda-Prejbeanu, M. Miron, and G. Gaudin, J. Appl. Phys. **112**, 053901 (2012).

[43] O. Boulle, L. D. Buda-Prejbeanu, E. Jué, I. M. Miron, and G. Gaudin, J. Appl. Phys. **115**, 17D502 (2014).

[44] L. Lopez-Diaz, D. Aurelio, L. Torres, E. Martinez, M. A. Hernandez-Lopez, J. Gomez, O. Alejos, M. Carpentieri, G. Finocchio, and G. Consolo, J. Phys. Appl. Phys. **45**, 323001 (2012).

[45] A. A. Thiele, Phys. Rev. Lett. **30**, 230 (1973).

[46] E. Martinez, S. Emori, N. Perez, L. Torres, and G. S. D. Beach, J. Appl. Phys. **115**, 213909 (2014).

[47] S. Emori, D. C. Bono, and G. S. D. Beach, J. Appl. Phys. **111**, 07D304 (2012).

[48] S. Lemerle, J. Ferré, C. Chappert, V. Mathet, T. Giamarchi, and P. Le Doussal, Phys. Rev. Lett. **80**, 849 (1998).

[49] P. J. Metaxas, J. P. Jamet, A. Mougin, M. Cormier, J. Ferré, V. Baltz, B. Rodmacq, B. Dieny, and R. L. Stamps, Phys. Rev. Lett. **99**, 217208 (2007).

[50] A. Hubert and R. Schafer, *Magnetic Domains: The Analysis of Magnetic Microstructures* (Springer, Berlin, 1998).

[51] W. F. Brown, *Micromagnetics* (Interscience Publishers, New York, 1963).

[52] A. J. Newell, W. Williams, and D. J. Dunlop, J. Geophys. Res. Solid Earth **98**, 9551 (1993).

[53] G. Bertotti, *Hysteresis in Magnetism: For Physicists, Materials Scientists and Engineers* (Academic, New York, 1998).

[54] W. H. Press, *Numerical Recipes in Fortran 90: The Art of Parallel Scientific Computing* (Cambridge University Press, New York, 1996).

[55] E. Martinez, J. Phys.: Condens. Matter **24**, 024206 (2012).

[56] S.-G. Je, D.-H. Kim, S.-C. Yoo, B.-C. Min, K.-J. Lee, and S.-B. Choe, Phys. Rev. B **88**, 214401 (2013).

[57] T. Suzuki, S. Fukami, N. Ishiwata, M. Yamanouchi, S. Ikeda, N. Kasai, and H. Ohno, Appl. Phys. Lett. **98**, 142505 (2011).

[58] While this manuscript was under review, a theoretical treatment predicting DW tilting was independently published by O. Boulle *et al.*, Phys. Rev. Lett. **111**, 217203 (2013).